

Absolute cross sections for the dipole-allowed transitions $30s\text{-}30p$ and $29d\text{-}30p$ in collisions between charged particles and Na Rydberg atoms

V. D. Irby, R. G. Rolfes,* O. P. Makarov, and K. B. MacAdam

Department of Physics and Astronomy, University of Kentucky, Lexington, Kentucky 40506-0055

M. I. Syrkín

State University of New York, Maritime College, 6 Pennyfield Avenue, Bronx, New York 10485

(Received 22 June 1995)

Collisions between charged particles and highly excited Na Rydberg atoms have been measured to continue a study of the projectile-velocity dependence of collisionally induced dipole-allowed and dipole-forbidden transitions. Experiments involving H^+ , H_2^+ , He^+ , and Ne^+ projectiles incident on $Na(30s)$ and $Na(29d)$ cover the projectile-velocity range from 1.6 to 10 times the mean orbital velocity of the excited electron. The ratio of the sum of the two largest dipole-allowed cross sections that depopulate an initial $30s$ state ($30s \rightarrow 30p$ and $30s \rightarrow 29p$) to the total depopulation cross section of $30s$ has been measured for reduced velocities ranging from 5 to 10. *Absolute* cross sections for the two dipole-allowed transitions $30s \rightarrow 30p$ and $29d \rightarrow 30p$, where large quantum defects play a significant role, are also presented. These exhibit characteristic velocity-dependent thresholds. The experimental data are in good agreement with close-coupling calculations that use an m -averaged dipole coupling to describe both allowed and forbidden channels. The results emphasize the importance of optically forbidden transitions and have implications in the study of astrophysical and laboratory plasmas.

PACS number(s): 34.60.+z, 34.80.Dp

I. INTRODUCTION

Experimental and theoretical studies of inelastic collisions between charged particles and matter play an important role in our understanding of plasma physics and astrophysical phenomena. Recent studies of nl change induced in highly excited Rydberg atoms by charged-particle impact have tested some of the physical assumptions used in the above disciplines. Of particular interest is the difference in the collisional coupling between the initial and final states at low and at high projectile velocities. At high velocities, the collisional interaction between a charged particle and a Rydberg atom exhibits a perturbative or "photonlike" character with transitions governed by the dipole selection rule $\Delta l = \pm 1$. However, when the projectile velocity becomes comparable to that of the initial orbital velocity of the electron, the interaction exhibits a behavior described by $|\Delta l| > 1$. In contrast with the above observations, collisional relaxation rates for plasma kinetics are traditionally obtained using only the dipole interaction, regardless of plasma temperature.

An example of the dominant collisional interaction at high projectile velocities is the recent work of Rolfes *et al.* [1]. Measurements carried out with electrons incident on $Na(30s)$ cover the range of reduced projectile velocities $\tilde{v} = v_p/v_e$ between 80 and 200 (where v_p is the projectile velocity and v_e is the mean orbital velocity of the $30s$ electron). The experimental results indicate that approximately 98% of the total depopulation of the initial $Na(30s)$ state is due to dipole-allowed transitions into the nearby $30p$ and

$29p$ states. Dipole-forbidden (i.e., $\Delta l > 1$) transitions are undetectable at these speeds. (A schematic diagram of the relevant energy levels of Na is given in Fig. 1).

On the other hand, an earlier study of Rolfes *et al.* [2] involving collisions between Na^+ projectiles and $Na(36s)$ targets, covering a reduced-velocity range $\tilde{v} = 0.6\text{--}1.4$, revealed that transitions were entirely dipole forbidden. Sublevels of the two nearest manifolds ($n = 34$ and 35 with $\Delta l \geq 2$) were populated almost uniformly by the collisions, and dipole-allowed transitions to nearby p states were not observed at all at those speeds. Further experimental measurements by Rolfes *et al.* [3], of the depopulation of $Na(30s)$ by He^+ impact, revealed that the ratio $R_{30s}(\tilde{v})$ of the sum of the cross sections for the dipole-allowed transitions ($30s \rightarrow 30p$ and $30s \rightarrow 29p$) to the total depopulation

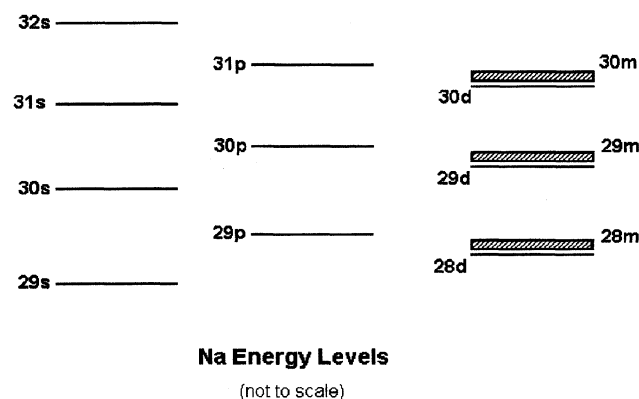


FIG. 1. Schematic diagram of the relevant energy levels of Na. $28m$, $29m$, and $30m$ represent manifold states with $l \geq 3$.

*Permanent address: Division of Science and Mathematics, Transylvania University, Lexington, KY 40508.

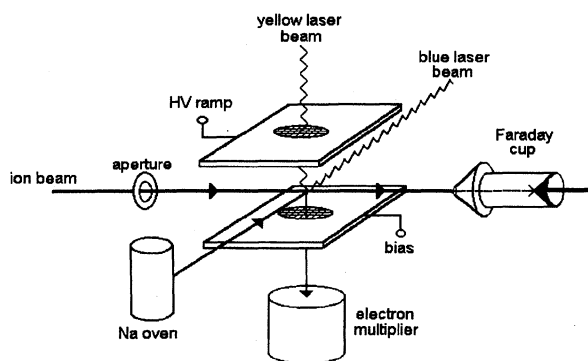


FIG. 2. Rydberg target-interaction region. The Faraday cup shown can be simultaneously translated in a direction parallel with the ion beam and parallel with the Na and blue laser beam. (See text.)

cross section increased from only 20% at $\tilde{\nu}=2.4$ to 65% at $\tilde{\nu}=5.6$.

In this work we have extended the measurements of the ratio $R_{30s}(\tilde{\nu})$ up to $\tilde{\nu}=10$ by bombarding Na(30s) with the lighter ions H^+ and H_2^+ . In addition, we have measured *absolute* cross sections for the dipole-allowed transitions Na(30s) to Na(30p), and Na(29d) to Na(30p), within the projectile-velocity range at which the coupling changes from predominantly dipole forbidden to dipole allowed. The experimental measurements, which were obtained by bombarding Na(30s) and Na(29d) with He^+ , and Ne^+ projectiles, cover the reduced projectile-velocity range from $\tilde{\nu}=1.6$ to $\tilde{\nu}=6$. The cross sections exhibit different projectile-velocity-dependent thresholds for the two dipole-allowed transitions. Absolute cross sections for the 30s \rightarrow 30p transition, which are less than $6 \times 10^{-10} \text{ cm}^2$ below $\tilde{\nu}=2.5$, increase gradually with projectile velocity, finally reaching a maximum of $15 \times 10^{-10} \text{ cm}^2$ near $\tilde{\nu}=6-8$. On the other hand, cross sections for the 29d \rightarrow 30p transition steeply rise at $\tilde{\nu}=2$, reaching a maximum value of $42 \times 10^{-10} \text{ cm}^2$ near $\tilde{\nu}=3-4$. The different appearance of the two cross sections is surprising, at first glance, since the average electron orbital radii and velocities are essentially the same for the initial 29d and 30s states. However, when energy defects are taken into account, the onsets or peaks of the two cross sections are in rough agreement with the Massey criterion [4]. Analytic estimates, which will be discussed in Sec. V, yield more realistic results. (The energy level separations between 30s \rightarrow 30p and 29d \rightarrow 30p are 135 and 43 GHz, respectively.)

A description of the experimental apparatus and data analysis are presented in Sec. II, followed by a discussion of the experimental results in Sec. III. Comparison of the data with close-coupling calculations and the normalized Born approximation are made in Sec. IV.

II. EXPERIMENTAL APPARATUS

Highly excited Rydberg target atoms used in this work are produced between two parallel condenser plates situated within the target-interaction region shown in Fig. 2. A thermal beam of Na is illuminated by two 5-ns pulsed dye lasers, which have a repetition rate of 20 Hz. The yellow laser (5890

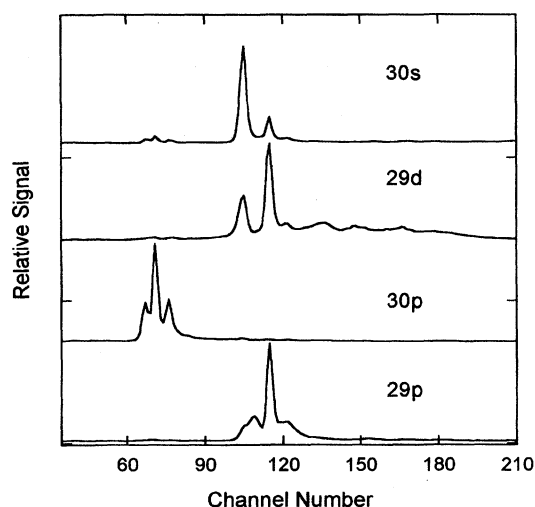


FIG. 3. Experimental SFI signals (ions off) for 30s, 29d, 30p, and 29p states. The slow rate of the high-voltage ramp, applied to the upper condenser plate, generated an electric field on the order of $100 \text{ V/cm } \mu\text{s}$ (each channel corresponds to 20 ns). Each trace was obtained by appropriately tuning the blue laser. (See text.)

\AA) induces the transition from the ground $3^2S_{1/2}$ state to the intermediate $3^2P_{3/2}$ state, while the blue laser (4106 \AA) populates the final Na(nl) state of interest. At approximately $4 \mu\text{s}$ after the flash of the lasers, following a period of exposure of the target to ions, a linear high-voltage ramp [5] is applied to the upper condenser plate for state-selective field ionization (SFI) of the Rydberg atoms [5,6]. The Na^+ ions are swept downward and pass through a fine mesh grid where they are detected by a discrete-dynode electron multiplier operated in current mode. Signals from the multiplier are recorded by an 8-bit 50-megasample-per-second transient digitizer.

Figure 3 illustrates typical SFI signals obtained for Na(30s) and Na(29d). The slow rate of the electric field between the condenser plates is approximately $100 \text{ V cm}^{-1} \mu\text{s}^{-1}$. Also included in Fig. 3 are SFI traces for 30p and 29p states, recorded to identify their signatures when they appear as collision products. In order to excite p states directly, a small pulsed electric field ($\approx 15 \text{ V cm}^{-1}$) is generated, by application of an appropriate potential to the lower condenser plate, during the flash of the lasers to induce Stark mixing. This pulse is then terminated before the high-voltage ramp. Hints of the 30p state can also be observed in the directly excited 30s and 29d profiles, and we believe that this is due to dipole transitions caused by blackbody radiation and/or Rydberg-Rydberg collisions in the target region. One should note that while the SFI signal of the 29p state overlaps the 30s and 29d states, the 30p state is well resolved from 30s and 29d.

Projectile ions used in this work are produced in a low-voltage discharge ion source. After extraction from the source, the ions pass through a Wien crossed-field velocity filter for mass selection and then through an ion-beam pulser, consisting of a set of deflection plates and an annular Faraday cup, before entering the Rydberg target-interaction re-

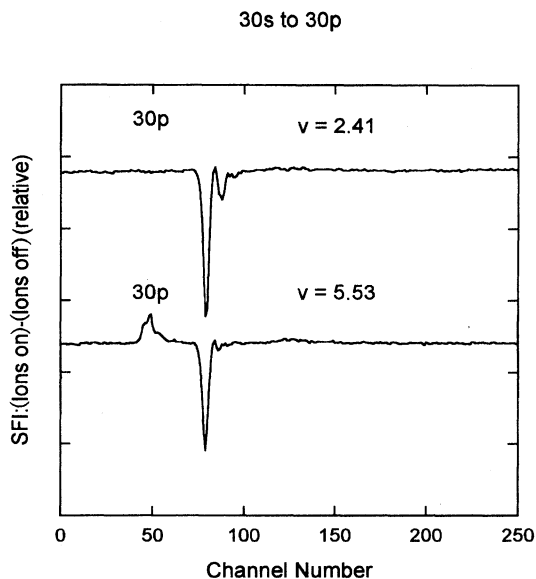


FIG. 4. Experimental measurements for He^+ incident on Na (30s) for reduced velocities of 2.41 and 5.53. The traces were obtained by subtraction of the SFI ions-off signal from the SFI ions-on signal and are offset above zero for clarity.

gion. The ion beam is “on” during the flash of the lasers. At 1–4 μs after the laser flash, an appropriately timed high-voltage pulse is applied to the deflection plates to effectively turn the ion beam “off.” Ions that pass through the target-interaction region are collected and monitored by the Faraday cup shown in Fig. 2.

Experimental data are obtained as follows. The blue laser is tuned to excite the desired 30s or 29d target state. With ions “on,” SFI traces are accumulated for 256 successive laser shots for a specific ion-target exposure time. The ion beam is then completely blocked, and SFI traces for ions “off” are accumulated for the same number of laser shots. The cycle of 256 successive laser shots for ions on/off is averaged over 20 repetitions. Following these measurements, the blue laser beam is blocked and ions on/off traces are obtained for background subtraction. The entire procedure is repeated for a variety of ion-target exposure times at each ion energy. Ion-beam densities are measured with the use of a small “translatable” Faraday cup *in situ* (see Fig. 2). The Faraday cup can be translated horizontally across the ion beam and is inserted into the target-interaction region for beam density measurements both immediately before and after accumulation of collision data. In addition to beam density measurements, SFI profile traces of 30p and 29p states are also taken (with ions “off”) for later data analysis.

Figures 4 and 5 illustrate Na(30s) and Na(29d) He^+ -impact SFI traces obtained by subtracting the background-corrected ions-off signal from the ions-on signal. The negative-going signal in each trace is indicative of the depopulation of the initial state. The pronounced increase in the 30p SFI signal in Fig. 4 when the reduced velocity increases from 2.41 to 5.53 is readily apparent. An appearance of Na(30p) in Fig. 5 as a collision product following bombardment of Na(29d) at higher velocities is likewise ap-

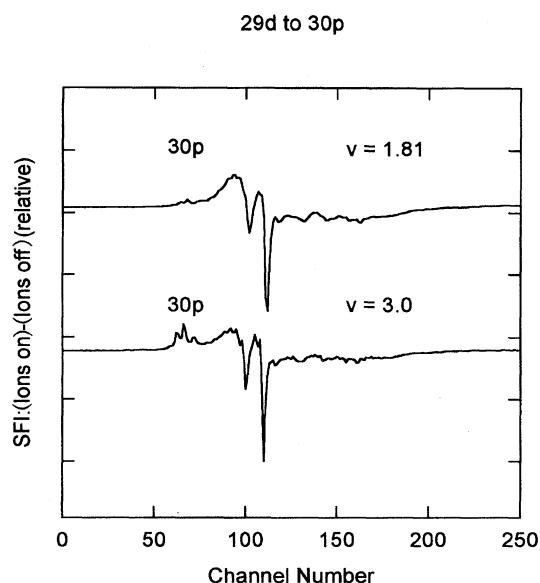


FIG. 5. Same as Fig. 4 except with Ne^+ and He^+ ions incident on Na(29d) at reduced velocities of 1.81 and 3.0, respectively.

parent, but in this case it arises at velocities as low as $\bar{v} = 3.0$.

Absolute cross sections for excitation of 30s and 29d to the 30p level can be obtained from the SFI ions-on (-off) traces by utilizing a slope method [7], which is described as follows. For single-collision conditions, the number $n(30p)$ of 30p atoms created by collisions is related to the number of atoms in the initial state $n(30s, 29d)$ (denoting either 30s or 29d) by

$$n(30p) = n(30s, 29d) \sigma j \Delta t, \quad (1)$$

where j is the ion-beam particle flux ($\text{ions s}^{-1} \text{cm}^{-2}$), Δt is the ion-target exposure time, and σ is the corresponding inelastic cross section. Due to ion travel time and fringing-field effects for ions exiting the beam pulser, the actual ion-target exposure time Δt is uncertain. By plotting the ratio $n(30p)/n(30s, 29d)j$ against the turn-on time t of the ion-beam cutoff pulse, however, σ can be obtained from the slope without knowledge of the actual ion-target exposure time.

The ratio $n(30p)/n(30s, 29d)$ is obtained by a six-parameter least-squares fit to the SFI ions-on and ions-off traces. Let S_{on} and S_{off} represent the full (256-channel) SFI signals obtained for a particular initial state (either 30s or 29d). Let functions P_i ($i = 1, \dots, 6$) defined over the 256 channels represent basis functions of the fit that match the SFI signals of the significant initial and final states. P_1 is the recorded ions-off signal of the initial state, normalized to unit area. P_2 and P_3 represent SFI profiles for 30p and 29p states, respectively. These are obtained from the measured profiles as illustrated in Fig. 3, after subtracting small linearly varying backgrounds in the first and last 20 channels of the 256-channel records, and the profiles are also unit normalized. The net collision signal S_{net} is obtained by subtract-

ing S_{off} from S_{on} (after similar background correction). Three unit-normalized Gaussian functions P_4 , P_5 , and P_6 are also constructed to represent adiabatic state-selective field ionization (ASFI) profiles for uniform populations of the $n=28$, 29, and 30 manifolds ($l \geq 2$), respectively. (For the $30s$ initial state, only two Gaussian profiles, corresponding to the 28 and 29 manifolds, were needed.) The half-maximum points of each Gaussian are selected, initially, to coincide with the peak positions of the ASFI profiles for the s and p states on either side of a particular manifold [3,8] and are subsequently adjusted to obtain the best fits. The fraction of each of the six basis-function profiles P_i in the net collision signal is then determined from the relation

$$S_{\text{net}}/\Sigma S_{\text{off}} = (x_1 - 1)P_1 + \sum_{i=2}^6 x_i P_i, \quad (2)$$

where x_i is the fraction of profile P_i in the fit. ΣS_{off} is a normalization factor and is obtained by summing the ions-off signal over channels 1–256. The ratio $n(30p)/n(30s, 29d)$ is then obtained from the fractional populations x_i given in Eq. (2).

Accurate assessment of the effective ion-beam particle flux is an essential requirement for measurement of the absolute cross sections. Beam fluxes were measured by scanning the small movable Faraday cup (aperture area 2.14 mm²) across the ion beam parallel to the thermal Na beam (see Fig. 2), starting at the intersection point between the blue and yellow laser beams. The ion beams had typical full-width-at-half-maximum of 4–6 mm. Due to the thermal drift speed of the Rydberg target atoms $v_{\text{drift}} \approx 1 \text{ mm } \mu\text{s}^{-1}$ across the ion beam, it was necessary to average the ion-beam density over the target drift length $\Delta x = v_{\text{drift}} t_{\text{max}}$, where t_{max} was taken to be the largest of the ion-target exposure times (≈ 1 –4 μs) for each set of data used to obtain σ from the slope method. The exposure times were in turn limited, in order to ensure single-collision conditions, by using beam cutoff times such that the target depopulation did not exceed 15%. By plotting the ratio $n(30p)/n(30s, 29d)$ obtained from Eq. (2) versus ion-beam cutoff time t , the effective duration Δt of ion-target exposure for each cutoff time could be obtained from the t intercept for use in Eq. (1). The ratio $n(30p)/n(30s, 29d)$ varied linearly with t provided that the depopulation fraction $(1 - x_1)$ was less than 20%. The final ion-beam density j , used in the determination of the absolute cross section, was then taken as the average of the ion-beam flux over the length Δx .

III. DISCUSSION OF DATA

Corrections for radiative decay of the initial $30s$ and $29d$ states are necessary in the final analysis [Eq. (1)]. Extrapolation of the calculations of Theodosiou [9] of $n=29$ and 30 (adjusted to 300 K) give radiative lifetimes $\tau = 20.1$, 24.1, and 127 μs for $29d$, $30s$, and $30p$, respectively. A straightforward analysis (under single-collision conditions) indicates that cross sections given by Eq. (1) should be multiplied by the correction factor C_0 .

$$C_0 = \exp(-\tau_0/\tau_i) \quad (3)$$

TABLE I. Measured absolute cross sections for $30s$ to $30p$ and $29d$ to $30p$ transitions. Statistical errors shown are the standard deviation of repeated measurements. Overall absolute error is estimated to be on the order of 25%. The results have been corrected for radiative lifetimes (see text).

Reduced velocity	Energy (eV)	Ion	Cross section (10^{-10} cm^2)
30s to 30p			
2.5	3777	Ne ⁺	5.5 ± 0.4
4.0	1934	He ⁺	9.6 ± 0.7
5.0	3021	He ⁺	12.2 ± 0.9
6.0	4351	He ⁺	14.8 ± 1.0
29d to 30p			
1.6	1511	Ne ⁺	11.3 ± 0.6
1.8	1934	Ne ⁺	17.7 ± 1.0
2.0	2359	Ne ⁺	20.7 ± 1.2
2.5	755	He ⁺	29.4 ± 1.6
3.0	1088	He ⁺	37.7 ± 2.1
4.0	1934	He ⁺	42.0 ± 2.4
5.0	3021	He ⁺	33.4 ± 1.9
6.0	4351	He ⁺	32.8 ± 1.8

where τ_i is the lifetime of the $29d$ or $30s$ initial state. Time $\tau_0 = 6.05 \text{ } \mu\text{s}$ is the time interval between the laser flash and the turn-on point of the high-voltage linear ramp. Using the extrapolated radiative lifetimes above, $C_0 = 0.74$ and 0.78 for the $29d$ and $30s$ cross sections, respectively. All reported cross sections have been corrected for radiative lifetimes in this fashion.

Absolute cross sections for collisional excitation of Na ($30s$) and Na($29d$) to the $30p$ level are presented in Table I. The uncertainties given there represent the standard deviation of repeated measurements. Overall error is estimated to be on the order of 25% due to shot-to-shot fluctuations in laser power, ion-beam instability, and difficulties in the determination of average ion-beam densities. The results given in Table I are plotted in Fig. 6. Also included in the figure are theoretical results from close-coupling calculations and the normalized Born approximation (see below). Previous experimental measurements of the depopulation of Na($30s$) by He⁺ impact (Rolfes *et al.* [3]) revealed that the ratio of the sum of the cross sections for the dipole-allowed transitions ($30s \rightarrow 30p$ and $30s \rightarrow 29p$) to the total depopulation cross section increased from only 20% at $\tilde{\nu} = 2.4$ to 65% at $\tilde{\nu} = 5.6$. We have extended these measurements to higher velocities by using H₂⁺ and H⁺ ions. The previous and present results are compared with close-coupling calculations in Fig. 7.

IV. NORMALIZED BORN APPROXIMATION AND CLOSE-COUPPLING METHOD

We have used semiclassical impact-parameter theory to model the measured inelastic processes. In the present calculations, a charged particle was assumed to move along a rectilinear classical trajectory while Rydberg electron transitions were treated by a previously developed quantum close-coupling method [10]. In addition, the measurements are also compared with the normalized Born approximation (NBA) [10–12].

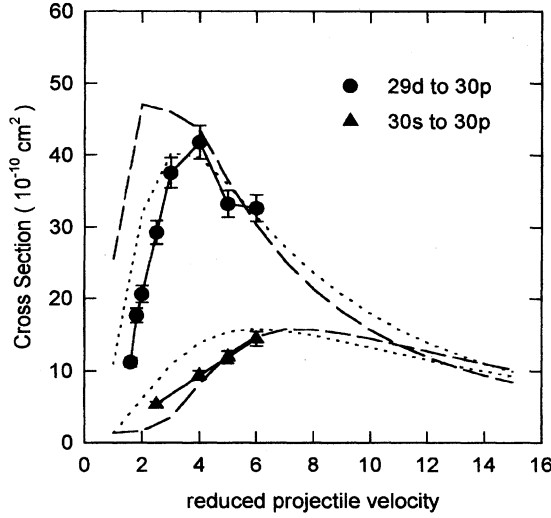


FIG. 6. Absolute cross sections as a function of reduced projectile velocity. Solid circles and triangles represent experimental results for the Na transitions $29d \rightarrow 30p$ and $30s \rightarrow 30p$, respectively. Dashed line indicates theoretical results obtained with the close-coupling method. Dotted line represents theoretical results obtained from the normalized Born approximation.

The cross section in the impact parameter (ρ) representation is given by

$$\sigma_{n_0 l_0 \rightarrow n l} = \int_0^\infty 2\pi\rho P_{n_0 l_0 \rightarrow n l}(\rho) d\rho. \quad (4)$$

In the NBA the probability $P_{n_0 l_0 \rightarrow n l}(\rho)$ is normalized to the total depopulation probability P_{tot} ,

$$P_{n_0 l_0 \rightarrow n l}(\rho) = \frac{P_{n_0 l_0 \rightarrow n l}}{1 + P_{\text{tot}}}, \quad (5)$$

where P_{tot} includes all channels that contribute to the depopulation of the initial level $n_0 l_0$. In particular, for the $30s \rightarrow 30p$ transition, the major normalization comes from $30s \rightarrow 30p$ and $30s \rightarrow 29p$ transitions. For $29d \rightarrow 30p$ the total probability includes mostly $29d \rightarrow 30p$ and $29d \rightarrow 29f$ transitions. All participating probabilities are given by the standard Born approximation for the dipole interaction (in a.u.), [10,11],

$$p_{n_0 l_0 \rightarrow n l} = (2d/\rho v)^2 \xi(\beta), \quad (6)$$

$$\xi(\beta) = \beta^2 [K_0^2(\beta) + K_1^2(\beta)], \quad (7)$$

$$\beta = \frac{\omega \rho}{v}, \quad (8)$$

where ω is the angular frequency for the transition from the initial $n_0 l_0$ state to the final $n l$ state, K_0 and K_1 are modified Bessel functions, and

$$d = \left(\frac{1}{2l_0 + 1} \sum_{m_{l_0}} | \langle n(l_0 \pm 1) m_{l_0} | z | n_0 l_0 m_{l_0} \rangle |^2 \right)^{1/2} \quad (9)$$

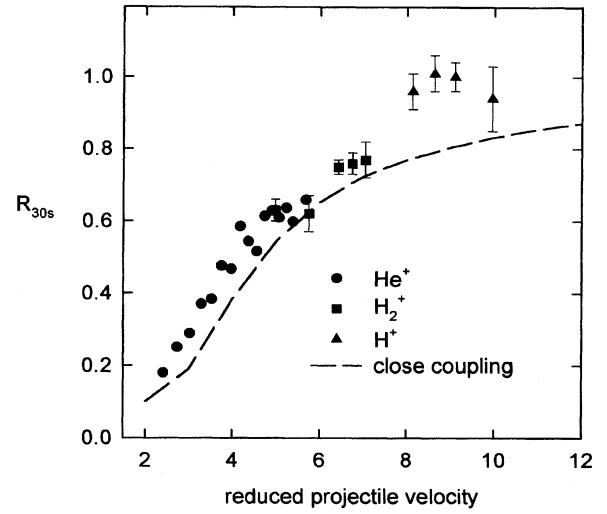


FIG. 7. Experimental measurements of the ratio R_{30s} of the sum of the dipole-allowed cross sections ($30s \rightarrow 30p$ and $30s \rightarrow 29p$) to the total depopulation cross section of the $30s$ initial state are plotted as a function of reduced projectile velocity. He^+ data (solid circles) are from Ref. [3]. Solid squares and solid triangles illustrate present experimental results for H_2^+ and H^+ , respectively. Dashed line indicates theoretical results obtained from close-coupling calculations.

is the dipole matrix element averaged over the azimuthal quantum numbers m_{l_0} . (All matrix elements were modified by nonhydrogenic corrections [13]). Cross sections obtained from Eq. (4) for the dipole-allowed transitions $30s \rightarrow 30p$ and $29d \rightarrow 30p$ are compared with the experimental results in Fig. 6. The NBA is in reasonable agreement with experiment for these optically allowed transitions.

However, the experimental results given in Fig. 7 indicate that at reduced velocities below $\tilde{v} = 3$ the collisional depopulation of $\text{Na}(30s)$ is dominated by dipole-forbidden transitions, most likely into the nearly $n = 28$ and 29 $l \geq 2$ manifolds [2]. As the velocity increases, the coupling between the initial and final states begins to change from predominantly dipole-forbidden to dipole-allowed. At reduced velocities above $\tilde{v} = 10$, the collisional interaction takes on a perturbative character with only dipole-allowed transitions occurring into the nearby $29p$ and $30p$ states. Thus, for low velocities, one must use a theoretical approach that allows for both dipole-allowed and dipole-forbidden transitions, such as the close-coupling method.

In the close-coupling method,

$$P_{n_0 l_0 \rightarrow n l}(\rho) = |a_{nl}(\rho, \infty)|^2, \quad (10)$$

where the quantum amplitudes $a_{nl}(\rho, \infty)$ come from integration of the time-dependent coupled Schrödinger equations,

$$i\dot{a}_{nl}(\rho, t) = \sum_{n'l'} e^{i\omega' t} V_{nl, n'l'}(\rho, v, t) a_{n'l'}(\rho, t), \quad (11)$$

where ω' is the angular frequency associated with the transition $n'l' \rightarrow nl$, and the m_l -averaged dipole potential $V_{nl, n'l'}(\rho, v, t)$ is given by

$$V_{nl,n'l'}(\rho, v, t) = d \frac{\rho + vt}{(\rho^2 + v^2 t^2)^{3/2}}. \quad (12)$$

This potential in particular reproduces the results of the NBA for fast collisions and has been found for slow collisions to reasonably describe transitions $\Delta l \geq 1$ between levels with small quantum defects [10,14]. We emphasize once again that the dipole coupling in Eq. (9) is the dominant interaction at these velocities and describes both dipole-allowed $\Delta l = 1$ and dipole-forbidden $\Delta l > 1$ transitions simultaneously: Each l state is coupled only to $l \pm 1$. However, all l 's are coupled together indirectly through Eq. (11) (see also Ref. [15]). As it is impractical to account for all possible participating levels in system (11), it is important to select correctly the *major* channels of depopulating transitions. The main contribution comes from $30s \rightarrow 30p \rightarrow 29d \rightarrow f \rightarrow g \rightarrow h$, and $30s \rightarrow 29p \rightarrow 28d \rightarrow f \rightarrow g \rightarrow h$. For $29d \rightarrow 30p$ we have incorporated also $30p \rightarrow 30s$ and $29d \rightarrow f \rightarrow g \rightarrow h$.

Cross sections obtained with the close-coupling method for the transitions $30s \rightarrow 30p$ and $29d \rightarrow 30p$ are presented and compared with the NBA and experiment in Fig. 6. The ratio of the sum of the dipole-allowed cross sections ($30s \rightarrow 30p$ and $30s \rightarrow 29p$) to the total depopulation cross section of the initial $30s$ state was also computed with the close-coupling method and is compared with experiment in Fig. 7. As the results in Fig. 7 illustrate, the fractional depopulation of Na($30s$), determined through the close-coupling method, is in reasonable agreement with experiment. For the absolute cross section measurements in Fig. 6, the close-coupling results are in better agreement with the $30s \rightarrow 30p$ transition than with $29d \rightarrow 30p$; in the latter case, the Born approximation is in better agreement. Our results confirm once again the reliability of the NBA for the quick assessment of optically allowed cross sections.

V. CONCLUSIONS

We have presented absolute cross-section measurements for the dipole-allowed Na transitions $30s \rightarrow 30p$ and $29d \rightarrow 30p$ induced by charged-particle impact for a wide range of projectile speeds above the matching velocity. The measurements are also in good agreement with results obtained from the normalized Born approximation and with present close-coupling calculations.

The experimental results exhibit characteristic onsets or peaks, in the two cross sections, which appear to be related to the corresponding energy defects and are in rough agreement with the Massey criterion. A more accurate assessment of the maximum cross sections can be made with use of the multilevel model [16]. Accordingly, the estimate for the re-

duced velocity at which the cross section exhibits a maximum is given by $\tilde{v}_m \approx (2d\Delta/n)^{1/2}$, where d is the dipole moment [Eq. (9)] and Δ is an appropriate difference of quantum defects equal to $\delta_s - \delta_p = 0.493$ for $30s \rightarrow 30p$, and $(1 - \delta_p) - \delta_d = 0.132$ for $29d \rightarrow 30p$. The resultant \tilde{v}_m are approximately 4.5 and 2.0, respectively, and compare more favorably with Fig. 6. The value of the cross-section maximum is given by $\sigma_m \approx C_0(\tilde{v}_m/\Delta)^2 \pi a_0^2 n^4$, where C_0 is the fraction of a given dipole channel in the total depopulation, equal approximately to $(1/2)(0.5)$ for $30s \rightarrow 30p$ according to Fig. 7 (Here the $30s \rightarrow 30p$ channel is approximately equal to the $30s \rightarrow 29p$ channel. Thus, the $30s \rightarrow 30p$ channel accounts for approximately $\frac{1}{4}$ of the total depopulation.) This results in $\sigma_m \approx 14 \times 10^{-10} \text{ cm}^2$, which is in good agreement with experimental results given in Fig. 6. (For the $29d \rightarrow 30p$ channel, the estimate is unclear since the depopulation fraction C_0 of this channel is unknown.)

The experimental results also confirm that the collisional depopulation of Na($30s$) is dominated by dipole-forbidden transitions at low projectile velocities. Thus, we have demonstrated explicitly that one must use a theoretical approach involving both optically allowed and forbidden transitions, such as the close-coupling method, to describe the collisional interaction at low projectile speeds. The dipole-forbidden transitions $|\Delta l| > 1$ appear to be caused solely by the dipole interaction and occur through chains of "virtual" dipole transitions $\Delta l = \pm 1$ [15]. There is good agreement between the present close-coupling calculations, which allow for these virtual transitions, and our experimental results for both dipole-allowed and -forbidden transitions.

One immediate implication of the above results is for collisional relaxation rates $\langle v\sigma \rangle$ for plasma kinetics, where $\langle \rangle$ denotes an average over the Maxwellian distribution of velocities in the plasma. Traditionally these rates were obtained in the dipole approximation based on different versions of perturbation theory regardless of plasma temperature. However, for ion temperatures $T_{\text{ion}}(\text{eV}) \lesssim (m_{\text{ion}}/m_{\text{electron}})(13.6/n^2)$, dipole-forbidden transitions can become a dominant process and should be accounted for by relevant calculations involving both dipole-allowed and -forbidden transitions. An example of such an approach was given, for small quantum defects, by Beigman and Syrkina [16], where analytic models were used within the close-coupling method to obtain dipole-forbidden cross sections and the corresponding relaxation rates.

ACKNOWLEDGMENT

This work was supported by NSF Grant No. PHY9122377.

- [1] R. G. Rolfes, L. G. Gray, O. P. Makarov, and K. B. MacAdam, *J. Phys. B* **26**, 2191 (1993).
- [2] R. G. Rolfes, L. G. Gray, and K. B. MacAdam, *J. Phys. B* **25**, 2319 (1992).
- [3] R. G. Rolfes, V. D. Irby, O. P. Makarov, R. C. Dickinson, and

- K. B. MacAdam, *J. Phys. B* **27**, 1167 (1994).
- [4] N. F. Mott and H. S. W. Massey, *Theory of Atomic Collisions* (Oxford University, London, 1949).
- [5] W. L. Fuqua III and K. B. MacAdam, *Rev. Sci. Instrum.* **56**, 385 (1985).

- [6] T. H. Jeys, G. W. Foltz, K. A. Smith, E. J. Beiting, F. G. Kellert, F. B. Dunning, and R. F. Stebbings, *Phys. Rev. Lett.* **44**, 390 (1980).
- [7] R. G. Rolfes, D. B. Smith, and K. B. MacAdam, *Phys. Rev. A* **37**, 2378 (1988).
- [8] K. B. MacAdam, L. G. Gray, and R. G. Rolfes, *Phys. Rev. A* **42**, 5269 (1990).
- [9] C. E. Theodosiou, *Phys. Rev. A* **30**, 2881 (1984).
- [10] I. L. Beigman and M. I. Syrkin, *Zh. Éksp. Teor. Fiz.* **89**, 400 (1985) [*Sov. Phys. JETP* **62**, 226 (1985)].
- [11] M. J. Seaton, *Proc. Phys. Soc.* **51**, 1105 (1963).
- [12] I. I. Sobel'man, L. A. Vainshtein, and E. A. Yukov, *Excitation of Atoms and Broadening of Spectral Lines* (Springer-Verlag, Berlin, 1981).
- [13] J. Picart, A. Edmonds, N. Tran Minh, and R. Pullen, *J. Phys. B* **12**, 2781 (1979).
- [14] X. Sun and K. B. MacAdam, *Phys. Rev. A* **47**, 3913 (1993).
- [15] I. C. Percival, in *Atoms in Astrophysics*, edited by P. G. Burke, W. B. Eissner, D. G. Hummer, and I. C. Percival (Plenum, New York, 1983), p. 75.
- [16] I. L. Beigman and M. I. Syrkin, *Kratk. Soobshcheniya Fiz.* **7**, 13 (1986) [*Sov. Phys. Lebedev Inst. Rep.* **7**, 21 (1986)].